PNAS
www.pnas.org

Supplementary Information for

The Carbon Content of Earth and its Core

Rebecca A. Fischer*, Elizabeth Cottrell, Erik Hauri, Kanani K.M. Lee, Marion Le Voyer

*Corresponding author: Rebecca A. Fischer
Email: rebeccafischer@g.harvard.edu

This PDF file includes:

Supplementary text
Figures S1 to S4
Tables S1 to S4
Legend for Dataset S1
SI References

Other supplementary materials for this manuscript include the following:

Dataset S1

www.pnas.org/cgi/doi/10.1073/pnas.1919930117

Supplementary Information Text

Unsuccessful experiments at lower pressures

It would be ideal to obtain metal–silicate partitioning data in the diamond anvil cell within the *P*–*T* range of large volume press data (and vice versa). However, we have made many attempts to do so and we have never once succeeded. The primary obstacle is that the temperature becomes extremely unstable when iron-bearing silicates are melted via laser heating at lower pressures, and the sample temperature often "runs away", increasing out of control at constant laser power. The temperature instabilities have numerous effects that render the experiments unusable, including making the temperature very difficult to measure; making it impossible to ensure that the sample was molten at the time of quench; and making it impossible to hold the sample at a constant temperature for any measurable length of time (<<1 second) to ensure equilibration. Very often large axial temperature gradients are produced due to an imbalance in temperature on the two sides of the sample. Fig. S4b documents the temperature evolution of a typical unsuccessful metal–silicate partitioning experiment from ~17 GPa performed in the Laboratory for Mineral Physics at Harvard University.

It is not entirely clear why laser-heating is so difficult at lower pressures, but we hypothesize that it may be due to a change in the properties of the subsolidus phase(s) across phase transitions (heating in the bridgmanite+ferropericlase stability field is far easier). The mineral–melt partitioning of iron can lead to runaway heating, as partial melting of the silicate (and metal–silicate reactions) partitions Fe into the melt, which causes the melt to absorb the laser more strongly, which raises the temperature and generates more melt and partitions more Fe into it, etc.

This is a near-universal problem in diamond anvil cell metal–silicate partitioning studies. There is generally no overlap in *P*–*T* space between diamond anvil cell and large volume press studies. The vast majority of diamond anvil cell metal–silicate partitioning studies only cover pressures above ~20–30 GPa (e.g., 23–24, 31, 36, 53, 57–61), with only one group as an exception to this trend (e.g., 62–65).

Comparison to previous studies of carbon metal–silicate partitioning

While we report a lower D_C than most previous studies, our values are not very different from three literature experiments at 10–15 GPa (19). They report D_C of 11, 21, and 31 at those pressures. We report D_C of 1–3 (NanoSIMS) or 8–35 (EPMA), with our lowest *P*–*T* experiment exhibiting the highest D_C (by EPMA or NanoSIMS). Metal–silicate partitioning of every element investigated so far, to our knowledge, exhibits some change with *P* and/or *T*, so it is expected that there would be some difference. The partition coefficient of Si (e.g., 23–24) changes by about the same amount as that of carbon (Fig. 2) between 1 bar and the high *P*–*T* of this study, for example.

We report a positive $1/T$ term, in agreement with virtually every previous study on carbon partitioning (e.g., 8, 16, 18–19, 22). Some previous studies did report a positive pressure trend, if any, but these studies only spanned a few GPa (e.g., 8, 14–18, 20). The previous studies that spanned the widest pressure range, a factor of ~2 greater (19, 21–22), found a negative pressure dependence, in agreement with our findings. The large volume press literature data (Dataset S1) appear to trend to lower D_C with increasing *P* and *T*, in agreement with our findings (Fig. S1).

Attainment of equilibrium

Experiments were held at the target laser power for 3 seconds (Materials and Methods; Fig. S4a). This should have been sufficient time to allow for metal–silicate equilibration. Time series and reversal experiments indicate that equilibrium is reached in <5 seconds in a multianvil press at ~5 GPa and $T >$ 2300 K (e.g., 66). At the much higher temperatures and smaller spatial scales of our experiments, equilibration should have occurred significantly faster than this. Our interpretation of equilibrium is also supported by the lack of compositional gradients or other heterogeneities (other than quench features) within both the metallic and silicate phases (e.g., 24).

Data compilation

We compiled a total of 100 measurements of the metal–silicate partitioning of carbon from the literature to combine with the present data (8, 14–20) (Fig. 2, S1; Dataset S1). For each experiment from the literature, we recalculated the partition coefficient $D_C = \frac{C_C^{metal}}{C_C^{silicate}}$, where C_C^{metal} and $C_C^{silicate}$ are the concentrations (in wt%) of carbon in the equilibrating metallic and silicate melts, respectively; the degree of silicate melt polymerization, NBO/T (67); and the oxygen fugacity in log units relative to the iron–

wüstite (IW) buffer under the approximation of ideality as $\Delta IW \approx 2 * \log\left(\frac{X_{FeO}^{silicate}}{X_{Fe}^{metal}}\right)$, where $X_{FeO}^{silicate}$ and X_{Fe}^{metal} are the mole fractions of FeO in the silicate melt and Fe in the metallic melt, respectively. Data from experiments equilibrated at oxygen fugacities below IW–4 were not used, due to a change in the sign of the dependence of partitioning on oxygen fugacity seen at around this value in the combined datasets of Armstrong et al. (14) and Li et al. (17). This should not impact our findings because Earth's core segregated predominantly at oxygen fugacities above IW–4 (e.g., 23, 28, 35, 51). We performed a stepwise, unweighted linear regression to the combined datasets, resulting in Eq. 1–2. Terms based on the water content of the silicate melt and silicon content of the metallic melt were found to be statistically insignificant at the 90% confidence level.

Carbon contents of the quenched silicate glass measured by EPMA versus NanoSIMS

Analyses of the carbon contents of the quenched silicate melts by EPMA and NanoSIMS differed, with EPMA measuring lower C contents. This is surprising, and the opposite trend than would be expected if EPMA measurements were affected by contamination or secondary fluorescence (e.g., 68) from the adjacent more carbon-rich quenched metallic melt. The carbon abundances measured by the two different techniques on the same samples are correlated: samples R187 and R195 exhibit the highest C abundances by both techniques, with R196 intermediate, and R193 exhibited the lowest C abundances by both techniques (Table S1). Despite this encouraging correlation, the discrepancy between the two techniques merits further exploration, and we offer four possible explanations.

The discrepancy may be due to the quench textures of the silicate glasses in these experiments. These silicate melts exsolved nano-scale metallic blebs upon quench, which have previously been ubiquitously reported in laser-heated diamond anvil cell metal–silicate partitioning studies and demonstrated to have been quench features on the basis of morphology and composition (e.g., 23–24, 36, 51, 57). Both EPMA and NanoSIMS quantification of carbon contents assumes a constant (glassy silicate) matrix, so the presence of these quench features may have affected either/both types of analysis. In the case of the NanoSIMS measurements, calibrations were constructed based on silicate glasses, and the level of inaccuracy introduced by applying this calibration to a mixed (mostly silicate glass, with some metal) matrix is unknown. In the case of the EPMA analysis of silicate, elements are calculated as oxides with assumed valence states. Because some Fe was present in metallic form and calculated as FeO, this introduces an unknown level of inaccuracy. However, the abundance of metallic quench blebs in the silicate melt (as visible in the EPMA; it is likely that some are <50 nm, e.g., 23, 36) is variable from sample to sample, yet all samples exhibit approximately the same degree of discrepancy between the EPMA and NanoSIMS carbon measurements.

The discrepancy may be due to two-dimensional heterogeneity in the glass. NanoSIMS analyses average over a larger two-dimensional area than the EPMA analyses: when using scanning ion imaging operation mode of the NanoSIMS, the composition of the entire silicate melt region (often an annulus several microns wide) was determined by averaging over a number of ROIs. The EPMA measurements are micron-scale, though multiple measurements were averaged. It is possible that this difference in measurement scale created a difference in the measured carbon contents due to the spatial heterogeneity in the samples' compositions (Fig. 1), though this is unlikely to produce the observed systematic bias.

The discrepancy may be due to three-dimensional sample heterogeneity. EPMA analyses produce an activation volume that typically extends 1–2 μm below the exposed sample surface, for silicates at these accelerating voltages. It is therefore possible that EPMA measurements include not only the quenched silicate melt but also unmelted materials (transformed silicates/oxides, starting materials, insulating media) from beneath the exposed surface. For samples polished parallel to the compression axis, the material below the quenched silicate glass was likely (Mg,Fe)O, the liquidus phase of the silicate. Ferropericlase measured adjacent to the quenched melt and metal had carbon contents below background (<0.3 wt.% carbon). For samples polished normal to the compression axis, the material below the quenched silicate glass was likely either the liquidus phase or the (~carbon-free) MgO pressure medium. In either geometry, the inclusion of subsurface materials within an activation volume could have systematically lowered the observed carbon content measured by EPMA. In contrast, NanoSIMS analyses are only sensitive to the thin surface layer being ablated, so measurements of the silicate melt by NanoSIMS did not contain any signal from other phases.

The discrepancy may be due to the linear extrapolation of the NanoSIMS calibration, which was based on glasses containing 45–1500 ppm. It has previously been shown that SIMS carbon calibrations are linear up to at least >2.4 wt% C when normalizing against ^{28}Si (50), and we expect similarly linear behavior when normalizing against ^{16}O (e.g., 50–52). However, if the calibration deviates from linear at higher carbon contents, that could potentially explain some of the difference between EPMA and NanoSIMS analyses.

In light of these possibilities, we prefer the carbon contents obtained by NanoSIMS. Because NanoSIMS places a surprisingly *lower* bound on the metal–silicate partition coefficients, we take the conservative approach of bracketing the carbon contents of the experiments with results from EPMA.

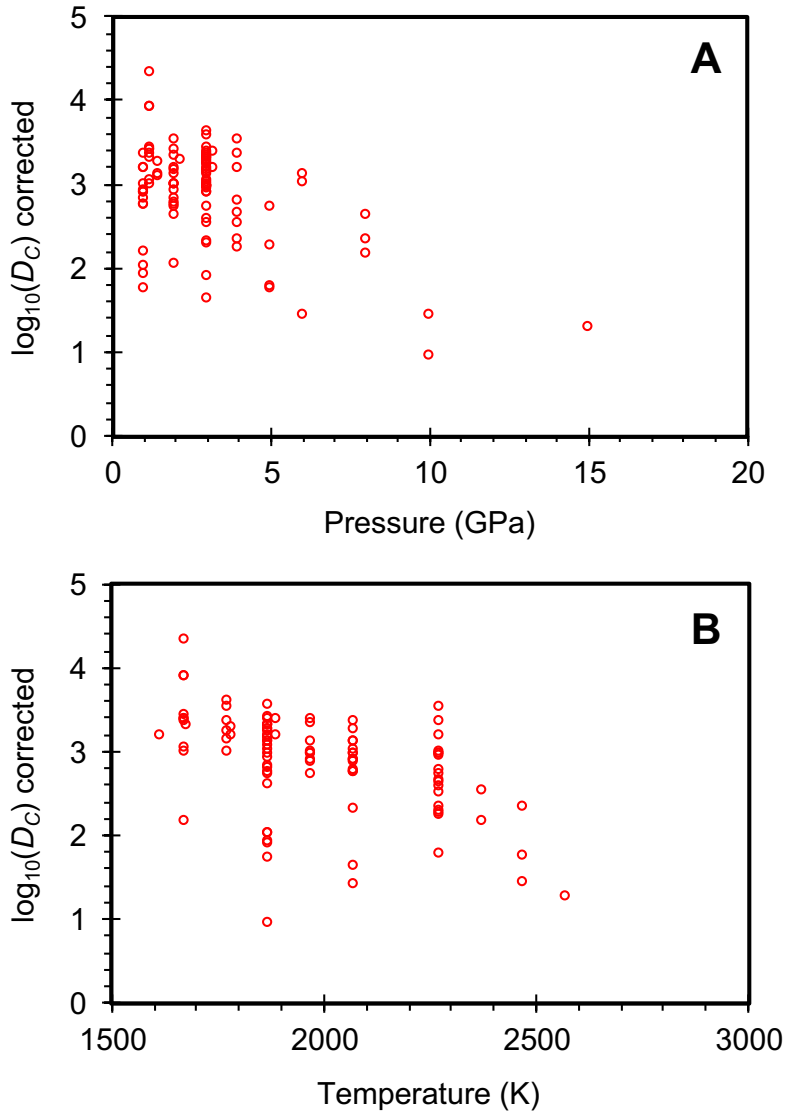

Fig. S1. Metal–silicate partition coefficients for carbon reported in previous studies (8, 14–20) (Dataset S1) as a function of pressure (A) or temperature (B). Data are corrected to a common NBO/T = 2.6, X_O = X_S = 0, and fO_2 = IW–2.2 using Eq. 2.

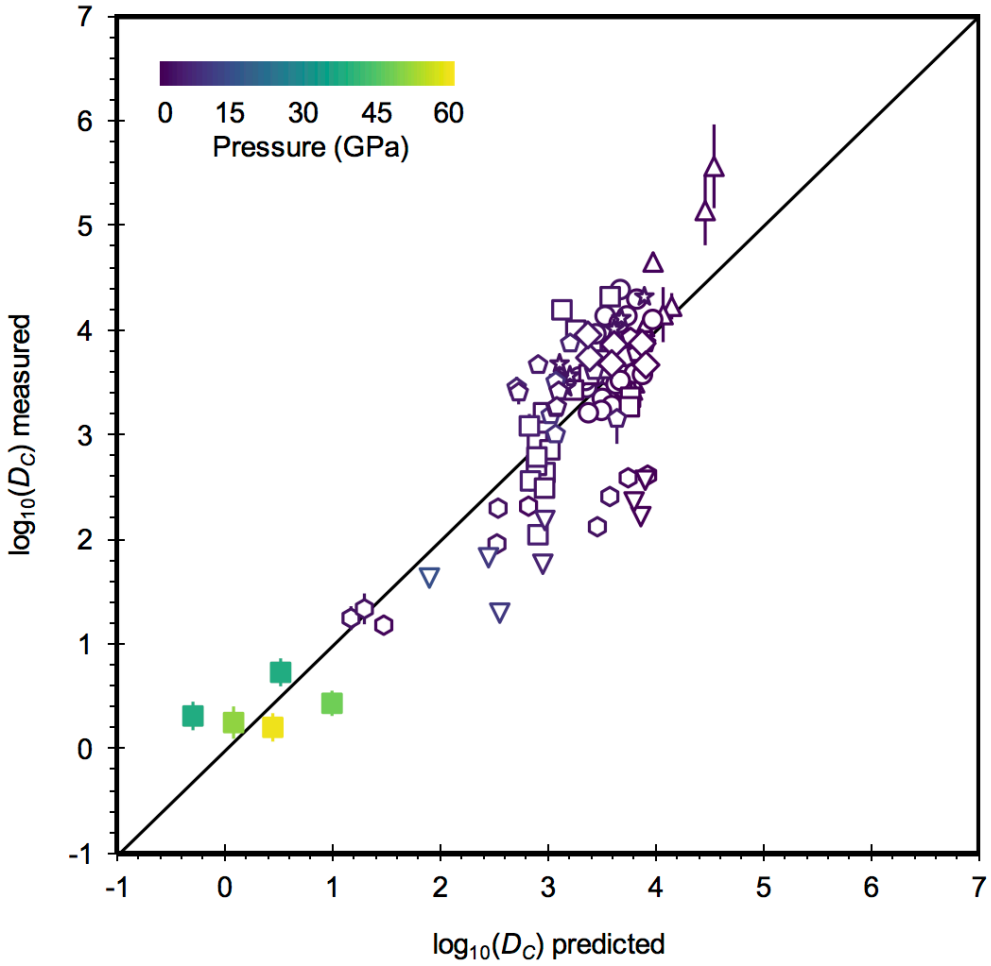

Fig. S2. Measured versus predicted (Eq. 1) metal–silicate partition coefficients for carbon from this study (filled squares) and previous studies (open symbols; Dataset S1). Data are color-coded by pressure. Triangles: 14. Circles: 15. Squares: 8. Hexagons: 16. Stars: 17. Pentagons: 18. Inverted triangles: 19. Diamonds: 20. Solid black line: 1:1 line. The root mean squared misfit is 0.5 log units.

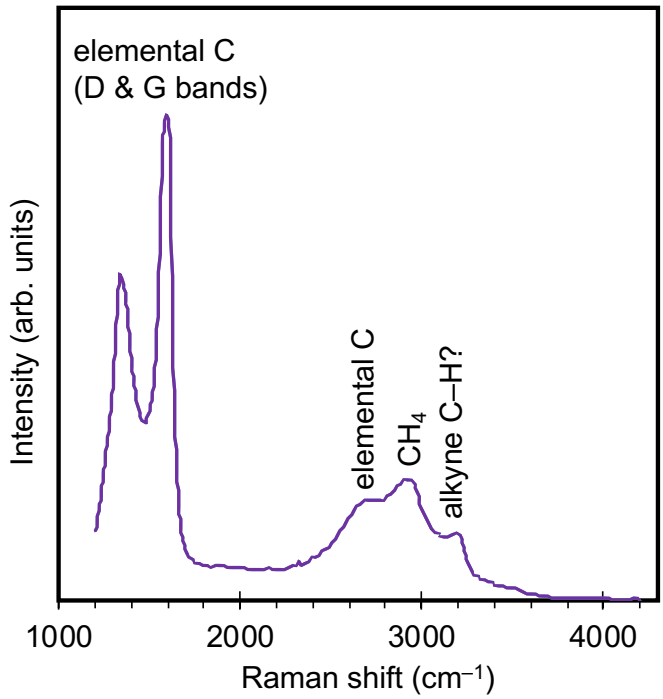

Fig. S3. Raman spectrum of the quenched silicate melt of sample R193, recovered from 37(7) GPa and 4350(450) K. Major volatile species are elemental carbon, CH_4, and alkyne C–H (Materials and Methods).

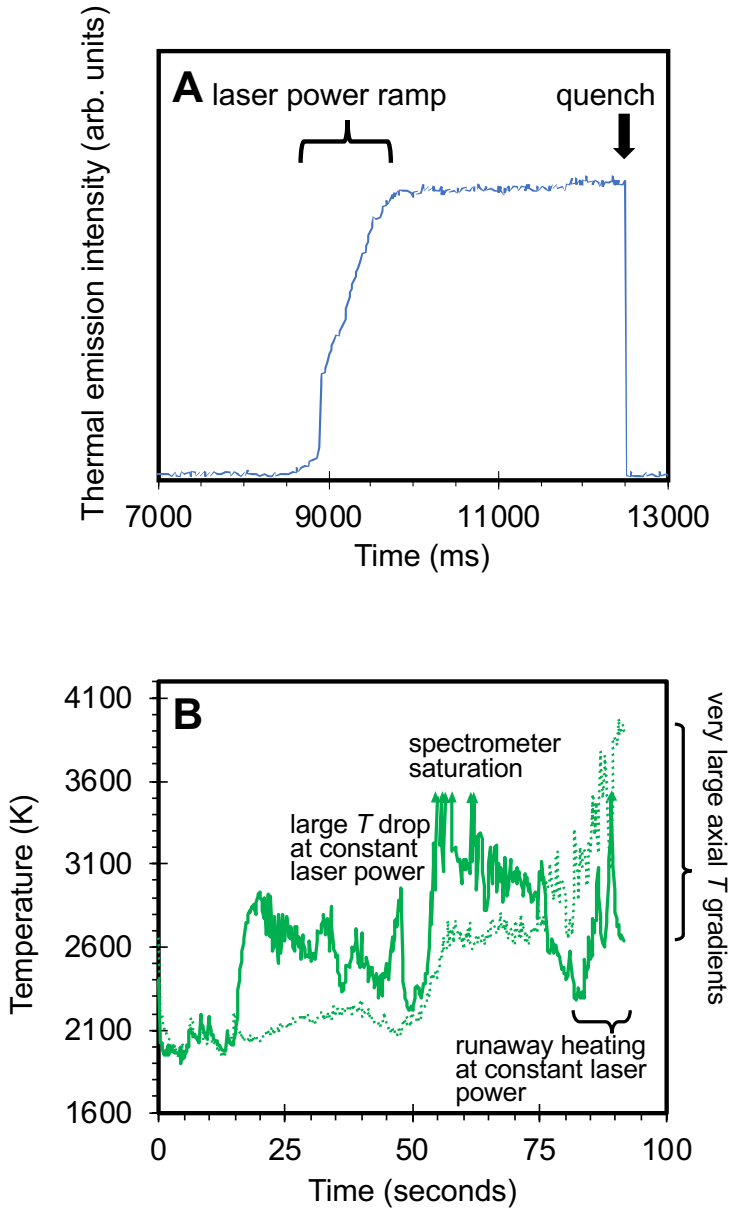

Fig. S4. Temperature evolution of some typical experiments. A: Temporal evolution of the thermal emission intensity (a proxy for temperature) during laser heating of successful experiment R196 at 37(8) GPa. The sample was held at peak laser power for 3 seconds before quench to allow for metal–silicate equilibration. No temperature instabilities or runaway heating occurred, and the temperature is very stable at constant laser power. B: Temperature evolution of an unsuccessful experiment from ~17 GPa, typical of all experiments attempted at pressures of <20–25 GPa. Solid and dotted lines are temperatures measured from the two sides of the sample. Arrows indicate saturation of the spectrometer, which corresponds to a temperature of >3500 K (solid lines). Laser power was increased with time, but the largest increases in temperature frequently occurred at constant laser power (runaway heating). Extreme instabilities in temperature and very large temperature gradients between the two sides occur. Note that the laser power–time history was different for these two experiments (A and B), but they exhibit very different behavior even at constant laser power.

Table S1. Pressure–temperature conditions and compositions (in wt%) of silicate melts determined by EPMA and NanoSIMS. Totals were determined using carbon measured by EPMA.

Sample	R187	R193	R195	R196	R202
Pressure (GPa)	50(9)	37(7)	59(10)	37(8)	47(8)
Temperature (K)	5150(500)	4350(450)	4200(400)	4950(500)	5200(500)
FeO	38.1(27)	24.2(6)	31.8(26)	42.5(31)	30.5(14)
NiO	0.92(27)	0.54(13)	0.32(4)	0.46(23)	–
Cr_2O_3	0.29(6)	0.18(3)	–	–	–
SiO_2	16.3(11)	32.7(14)	33.4(3)	11.8(7)	26.8(8)
MgO	40.2(20)	38.1(10)	31.6(14)	42.7(25)	34.2(8)
C (EPMA)	0.86(50)	0.22(11)	0.80(15)	0.64(16)	–
EPMA Total (carbon as CO)†	97.8(20)	96.3(5)	99.0(23)	99.0(12)	91.5(7)*
EPMA Total (carbon as C)†	96.7(18)	96.0(5)	98.0(23)	98.1(11)	91.5(7)*
EPMA Total (carbon as CH_4)†	97.0(18)	96.1(5)	98.2(23)	98.3(11)	91.5(7)*
C (NanoSIMS)	5.8(19)	2.3(5)	6.6(15)	4.1(10)	2.6(6)

†We obtain negligible differences in the EPMA totals depending on whether carbon in the silicate melt speciates predominately as CO, C, CH_4, or a combination of these. All three species are evident in our Raman spectra, but relative abundances cannot be determined. Moreover, the extent to which carbon speciation in the quenched glass faithfully records carbon speciation in the melt at pressure and temperature is unknowable. Our Raman spectra are consistent with previously published results for carbon species observed in glasses quenched from high *P*–*T* under reducing conditions (e.g., 14); knowledge of the balance of carbon species in the melt is not required for our calculations or interpretations.
*Total without carbon

Table S2. Pressure–temperature conditions and compositions (in wt%) of metallic melts determined by EPMA.

Sample	R187	R193	R195	R196	R202
Pressure (GPa)	50(9)	37(7)	59(10)	37(8)	47(8)
Temperature (K)	5150(500)	4350(450)	4200(400)	4950(500)	5200(500)
Fe	77.4(14)	76.5(28)	68.8(28)	82.1(14)	81.2(6)
Ni	2.47(23)	2.46(45)	0.43(4)	1.38(9)	0.55(7)
Cr	0.32(1)	0.23(2)	0.06(1)	–	–
Si	1.12(3)	0.31(6)	5.73(40)	0.68(8)	3.15(10)
Mg	2.17(4)	0.15(3)	1.94(5)	1.39(6)	1.15(4)
O	6.2(1)	1.9(4)	7.9(4)	4.8(4)	5.3(1)
C	7.5(5)	7.8(9)	7.7(5)	6.0(5)	4.9(4)
Total	97.2(19)	89.3(31)	92.6(27)	96.4(15)	96.3(9)

Table S3. Covariance matrix to fit of carbon metal–silicate partitioning data, as described by Eq. 1 (using NanoSIMS analyses of carbon in the silicate glass).

	Intercept	$1/T$ (K)	P/T (K/GPa)	$\log_{10}(1-X_O)$	NBO/T	$\log_{10}(1-X_S)$	fO_2 ($/\Delta$IW)
Intercept	0.490	–749	–23.1	–0.855	–0.0155	0.134	0.0272
$1/T$ (K)	–749	1234000	35170	999	20.9	–133	–22.2
P/T (K/GPa)	–23.1	35170	3565	384	0.669	–0.149	0.506
$\log_{10}(1-X_O)$	–0.855	999	384	79.0	0.172	0.675	0.229
NBO/T	–0.0155	20.9	0.669	0.172	0.00180	–0.00530	–0.00073
$\log_{10}(1-X_S)$	0.134	–133	–0.149	0.675	–0.00530	1.98	0.0178
fO_2 ($/\Delta$IW)	0.0272	–22.2	0.506	0.229	–0.00073	0.0178	0.00848

Table S4. Covariance matrix to fit of carbon metal–silicate partitioning data, as described by Eq. 2 (using EPMA analyses of carbon in the silicate glass).

	Intercept	$1/T$ (K)	P/T (K/GPa)	$\log_{10}(1-X_O)$	NBO/T	$\log_{10}(1-X_S)$	fO_2 ($/\Delta$IW)
Intercept	0.548	–837	–26.9	–1.69	–0.0191	0.148	0.0289
$1/T$ (K)	–837	1368000	40860	2227	26.1	–151	–24.1
P/T (K/GPa)	–26.9	40860	3908	455	0.909	–0.813	0.468
$\log_{10}(1-X_O)$	–1.69	2227	455	97.3	0.236	0.523	0.222
NBO/T	–0.0191	26.1	0.909	0.236	0.00208	–0.00614	–0.00081
$\log_{10}(1-X_S)$	0.148	–151	–0.813	0.523	–0.00614	2.05	0.0186
fO_2 ($/\Delta$IW)	0.0289	–24.1	0.468	0.222	–0.00081	0.0186	0.00879

Dataset S1 (separate file). Compilation of literature data used in the present study. Data were taken from (8, 14–20). Oxygen fugacity (fO_2) was calculated under the approximation of ideality. NBO/T was calculated using the method of (67). Corrected values of $\log_{10}D_C$ were calculated using Eq. 2 (corrected to NBO/T = 2.6, IW–2.2, and $X_O = X_S = 0$). Both corrected and uncorrected data are shown in Fig. 2. Only data more oxidized than IW–4 were used.

References

57. J. Badro, J. Siebert, F. Nimmo, An early geodynamo driven by exsolution of mantle components from Earth's core. *Nature* 536, 326–328 (2016).
58. I. Blanchard, J. Siebert, S. Borensztajn, J. Badro, The solubility of heat-producing elements in Earth's core. *Geochem. Persp. Let.* 5, 1–5 (2017).
59. B. A. Chidester, Z. Rahman, K. Righter, A. J. Campbell, Metal–silicate partitioning of U: Implications for the heat budget of the core and evidence for reduced U in the mantle. *Geochim. Cosmochim. Acta* 199, 1–12 (2017).
60. B. Mahan, J. Siebert, I. Blanchard, S. Borensztajn, J. Badro, F. Moynier, Constraining compositional proxies for Earth's accretion and core formation through high pressure and high temperature Zn and S metal–silicate partitioning. *Geochim. Cosmochim. Acta* 235, 21–40 (2018).
61. B. Mahan, J. Siebert, I. Blanchard, J. Badro, E. Kubik, P. Sossi, F. Moynier, Investigating Earth's formation history through copper and sulfur metal–silicate partitioning during core–mantle differentiation. *J. Geophys. Res.: Solid Earth* 123, 8349–8363 (2018).
62. R. M. G. Armytage, A. P. Jephcoat, M. A. Bouhifd, D. Porcelli, Metal–silicate partitioning of iodine at high pressures and temperatures: Implications for the Earth's core and ^{129}*Xe budgets. *Earth Planet. Sci. Lett.* 373, 140–149 (2013).
63. M. A. Bouhifd, A. P. Jephcoat, The effect of pressure on partitioning of Ni and Co between silicate and iron-rich metal liquids: a diamond-anvil cell study. *Earth Planet. Sci. Lett.* 209, 245–255 (2003).
64. M. A. Bouhifd, A. P. Jephcoat, Convergence of Ni and Co metal–silicate partition coefficients in the deep magma-ocean and coupled silicon–oxygen solubility in iron melts at high pressures. *Earth Planet. Sci. Lett.* 307, 341–348 (2011).
65. M. A. Bouhifd, D. Andrault, N. Bolfan-Casanova, T. Hammouda, J. L. Devidal, Metal–silicate partitioning of Pb and U: Effects of metal composition and oxygen fugacity. *Geochim. Cosmochim. Acta* 114, 13–28 (2013).
66. Y. Thibault, M. J. Walter, The influence of pressure and temperature on the metal–silicate partition coefficients of nickel and cobalt in a model C1 chondrite and implications for metal segregation in a deep magma ocean. *Geochim. Cosmochim. Acta* 59, 991–1002 (1995).
67. B. O. Mysen, D. Virgo, F. A. Seifert, The structure of silicate melts: Implications for chemical and physical properties of natural magma. *Rev. Geophys. Space Phys.* 20, 353–383 (1982).
68. J. Wade, B. J. Wood, Metal–silicate partitioning experiments in the diamond anvil cell: A comment on potential analytical errors. *Phys. Earth Planet. Inter.* 192–193, 54–58 (2012).